Diffusion-mediated growth and size-dependent nanoparticle reactivity during Ruthenium Atomic Layer Deposition on dielectric substrates

Job Soethoudt[1,2]*, Fabio Grillo[3]*, Esteban A. Marques[3], J. Ruud van Ommen[3], Yoann Tomczak[2†], Laura Nyns[2], Sven Van Elshocht[2], Annelies Delabie[1,2]

1 Department of Chemistry, KU Leuven (University of Leuven), 3001, Leuven, Belgium

2 Imec, Kapeldreef 75, 3001, Leuven, Belgium

3 Department of Chemical Engineering, Delft University of Technology, 2629 HZ, Delft, The Netherlands

ABSTRACT: Understanding the growth mechanisms during the early stages of atomic layer deposition (ALD) is of interest for several applications including thin film deposition, catalysis, and area-selective deposition. We investigated the surface dependence and growth mechanism of (ethylbenzyl)(1-ethyl-1,4-cyclohexadienyl)ruthenium (EBECHRu) and O_2 ALD at 325°C on HfO_2, Al_2O_3, -OH and Si-O-Si terminated SiO_2, and organosilicate glass (OSG). Our experimental results show that precursor adsorption is strongly affected by the surface termination of the dielectric, and proceeds most rapidly on -OH terminated dielectrics, followed by Si-O-Si and finally $Si-CH_3$ terminated dielectrics. The initial stages of growth are characterized by the formation and growth of Ru nanoparticles, which is mediated by the diffusion of Ru species. Mean-field and Kinetic Monte Carlo modeling show that ALD on OSG is best described when accounting for (1) cyclic generation of new nanoparticles at the surface, (2) surface diffusion of both atomic species and nanoparticles, and (3) size-dependent nanoparticle reactivity. In particular, our models indicate that precursor adsorption initially occurs only on the dielectric substrate, and occurs on the Ru nanoparticles only when these reach a critical size of about 0.85 nm. This phenomenon is attributed to the catalytic decomposition of oxygen requiring a minimum Ru nanoparticle size.

Introduction

In Atomic Layer Deposition (ALD), materials are deposited from gas phase precursors on a substrate by a cyclic process consisting of two or more alternating self-limiting surface reactions. These self-limiting surface reactions enable thin-film deposition with thickness uniformity over large-area substrates, (sub-) monolayer thickness control, and conformal deposition in 3D structures[1]. During the first ALD cycles the precursors mainly react with the substrate rather than with the ALD-grown material. The surface termination of the substrate can therefore strongly affect the growth behavior during this initial period[1-3]. Depending on the nature of the ALD-grown material, the substrate, and the process conditions, ALD can lead to different growth regimes, resulting for instance in the deposition of ultra-thin continuous films, deposition of highly dispersed nanoparticles, or area-selective deposition[4]. Continuous thin films have a wide variety of applications including nano-electronics, coatings, and optical components, and their deposition requires either two-dimensional growth or high particle density to achieve fast film closure. Nanoparticles dispersed on a surface are desired for heterogeneous catalysis, and their production requires island-type deposition with a well-defined particle size and particle density. Area-selective deposition can enable nanoscale bottom-up patterning, which allows accurate self-alignment between small features which is difficult to achieve in conventional top-down patterning[5]. To enable area-selective deposition, the growth behavior should be surface-dependent such that the deposition is at the same time favored on designated areas of the substrate and inhibited on others. For each of the aforementioned applications, an understanding of the surface dependence of the initial stages of growth can inform the tailoring of the ALD process to the desired application[6].

ALD of noble metals has received considerable attention because of its potential in applications such as catalysis[7] and nano-electronic devices[8]. Ruthenium is considered an ideal candidate for novel nanoscale catalysts[9,10] as well as for replacing copper as a conductor in future low-level nano-interconnect structures for integrated circuits[8]. ALD of Ru however presents application-specific challenges. On one hand, nanoparticles of a specific size are desired for high catalytic activity[10]. On the other hand, Ru interconnects require conformal deposition inside ultra-small 3D features that often results in void or seam formation, leading to increased resistance and poor electromigration performance[11]. Void formation may be prevented by a bottom-up fill of the 3D feature, which requires area-selective deposition of Ru on the bottom of the feature (typically a metal from the lower-lying conductor) and not on the sidewalls (typically a dielectric). Indeed no barrier layer is needed when using Ru as an interconnect[8], allowing the bottom and the sidewall of a feature to consist of different surfaces which in turn may enable an area-selective approach.

The surface dependence of Ru ALD has been reported for a variety of processes[12-15], yet the underlying growth mechanisms are often not well understood. Long inhibition periods are common for Ru ALD, especially in processes based on combustion reactions[16]. Inhibition occurs on dielectric surfaces for a variety of O_2-based processes such as bis(ethylcyclopentadienyl)ruthenium/O_2 and (ethylcyclopentadienyl)(pyrrolyl)ruthenium/O_2 ALD, because the catalytic decomposition of oxygen does not occur on dielectric substrates[16,17]. In contrast, almost immediate linear growth on SiO_2 substrates has been reported for ALD processes using zerovalent Ru precursors and O_2. This precursor type appears to display increased reactivity towards dielectric surfaces, yet the precise difference in surface reactions for different precursor types was not reported. ALD processes using zerovalent precursors yield smooth Ru films with low resistivity values of 14 $\mu\Omega$cm at 15nm thickness[12,18-20]. The short inhibition period observed for these precursors is linked to fairly high initial particle densities of 10^{12} cm^{-2} [12,19]. However, the growth mechanism for ALD processes based on zerovalent Ru precursors has to the best of our knowledge not yet been reported.

Recent studies have shown that ALD of metals can be affected by non-equilibrium phenomena such as surface diffusion of nanoparticles, adatoms, and (partially decomposed) precursors[21-23]. In particular, kinetic processes such as dynamic coalescence can have a great impact on the evolution of the particle size distribution (PSD) throughout the deposition process. Surface diffusion during noble metal ALD can be promoted by differences in surface energy between the dielectric substrate and the deposited metal. Such a driving force is also expected to influence Ru ALD on dielectrics, favoring Ru aggregation through surface area minimization (compare surface energies of 3.05 J/m^2 for Ru vs 0.0518 J/m^2 for SiO_2[24,25]). When surface diffusion plays a crucial role in the growth mechanism, the particle size and particle density evolution cannot be predicted from the particle density in the first cycle as in the model proposed by Puurunen and Vandervorst for dielectric ALD[26]. Instead the effect of diffusion on the particle size distribution should be taken into account, such as in the recent combined modeling/experimental study of Pt ALD[21,27,28]. Another possibility which should be taken into account is that the generation of new nanoparticles is spread out in time - or in ALD, over many cycles[29]. The possibility of cyclic nanoparticle generation should therefore also be considered when determining the initial growth mechanism.

As widely reported in the field of catalysis, the catalytic activity of supported noble metal nanoparticles is often strongly dependent on nanoparticle size as well as the surface structure of the nanoparticle[30-32]. In particular, the catalytic dissociation of oxygen by the Ru surface is known to play a role in the combustion reaction of the ligands for Ru ALD[16], and the dissociation of O_2 on supported Ru nanoparticles has been reported to be size-dependent[33]. This size-dependent nanoparticle reactivity may play a pivotal role in Ru ALD growth mechanisms especially when O_2 is used as a coreagent, yet to the best of our knowledge this aspect has not been taken into account in the description of nanoparticle growth mechanisms during Ru ALD.

In this work, we report on the surface dependence and growth mechanism of Ru ALD from the (ethylbenzyl)(1-ethyl-1,4-cyclohexadienyl)ruthenium (EBECHRu) precursor and oxygen on several dielectric surfaces. First, we discuss the surface dependence of the amount of material deposited during the initial cycles. Subsequently, we present a detailed study of the growth mechanism based on the evolution of the size and density of the Ru nanoparticles with the number of cycles. The initial growth behavior on organosilicate glass is simulated by a modified version of the ALD growth model proposed by Grillo et al.[21,27],which accounts for cyclic nanoparticle generation, size-dependent nanoparticle diffusion, and size-dependent nanoparticle reactivity. Finally, the implications for both EBECHRu/O_2 ALD in particular and noble metal ALD in general are discussed. This combined experimental-theoretical approach provides new fundamental insight into the growth mechanism during the early stages of ALD.

Experimental methods

The substrates are prepared on 300mm Si (100) wafers. Five different dielectric surfaces are considered as substrates for Ru ALD: A hydrophilic SiO_2 surface is obtained by Plasma-Enhanced ALD (PEALD) of 10nm SiO_2 at 75°C. A hydrophobic SiO_2 surface is obtained by growing 90nm dry thermal SiO_2 at 1000°C. An Organosilicate Glass (OSG) surface is obtained by Plasma-Enhanced Chemical Vapor Deposition (PECVD) of 100nm OSG film with a density of 1.35 g/cm^3 and k-value of 2.8. HfO_2 and Al_2O_3 layers are deposited on SiO_2. The HfO_2 surface is obtained by 2nm $HfCl_4$/H_2O ALD at 300°C, and 2nm Al_2O_3 is deposited through $Al(CH_3)_3$/H_2O ALD at 300°C. Each substrate is brought to the ALD reactor immediately after preparation to minimize the effect of air exposure.

Ruthenium is deposited on each of the aforementioned surfaces by alternating EBECHRu and O_2 pulses in an ASM Pulsar 3000 cross-flow reactor connected to a Polygon platform. The temperature of the substrate susceptor is kept at 325°C, as EBECHRu/O_2 ALD at 325°C is reported to yield films with high crystallinity, low resistivity, and low impurity content[19,20]. The substrates are first stabilized on the susceptor for 5 minutes to desorb moisture or other contaminants before ALD. An EBECHRu/O_2 ALD cycle consists of a 5s EBECHRu pulse, 5s N_2 purge, 0.4s O_2 pulse, and 3s N_2 purge. A varying number of ALD cycles ranging from 0 to 800 has been applied to study the growth behavior. In some cases, substrates were exposed to pulses of O_2 and H_2O to study how these reagents may affect the surface terminations and subsequent Ru ALD.

Some SiO_2 and OSG substrates are subjected to surface characterization. The surface hydrophobicity is measured by Water Contact Angle (CA) using a Dataphysics OCAH 230 tool. The surface density of –OH groups is quantified by allowing each surface -OH group to react with a single $HfCl_4$ molecule, and subsequently measuring the Hf areal density. This approach is explained in detail elsewhere, and gives a reasonable indication of the surface density of –OH groups in a range of 0.04 - 0.29·10^{15} -OH/cm^2 [34]. In this approach, the surface is exposed to one $HfCl_4$/H_2O ALD cycle at 300°C starting with one second of $HfCl_4$ exposure. We presume

that this chemisorption reaction deposits one Hf atom on the surface for each -OH group originally present. The areal density of Hf is then obtained by Rutherford Backscattering Spectrometry (RBS) using a 1.523 MeV He+ incoming ion beam. In the OSG film, functional groups are identified by Fourier Transformed Infrared spectroscopy in Attenuated Total Reflectance mode (ATR-FTIR) in a Nicolet 6700 spectrometer from Thermoelectron Corporation.

Samples cleaved from the center of the wafer are analyzed after Ru ALD. The increase in Ru coverage on each surface is measured by RBS using a 1.523 MeV He+ incoming ion beam. In some cases where a low areal density of Ru is expected, Ru coverage is instead determined by Total X-Ray Fluorescence Spectroscopy (TXRF) in a Rigaku TXRF300 tool with a high energy (24 keV) beam for heavy element detection. The particle density and growth behavior are investigated by top-view Scanning Electron Microscopy (SEM) using a FEI Helios 460 microscope. To obtain particle size distributions, the radius of each particle is calculated from its area assuming a circular shape. Because the smallest particles are difficult to reliably discern from SEM images, particles with an area smaller than 1 nm^2 in area are not considered in the distributions. The height of Ru particles was obtained by Atomic Force Microscopy (AFM) using a Bruker Dimension Icon PT tool and a OMCL-AC160TS probe tip in tapping mode. The speed at which Ru covers the SiO$_2$ and OSG surfaces is investigated using static Time of Flight Secondary Ion Mass Spectrometry (TOFSIMS) in combination with RBS. Positive ion intensities are measured with a TOFSIMS IV instrument from ION-TOF GmbH in dual beam configuration, using a Bi^{3+} gun at 25keV as a source. TOFSIMS can be used to study film closure because Ru coverage of the substrate increases with ALD cycle number. The surface of the dielectric substrate will therefore be increasingly less exposed, and fewer substrate Si ions will be collected. The rate of decay for the detected Si intensity with increasing Ru detected by RBS will depend on how rapidly the Ru film covers the substrate, and is therefore used to compare film closure speed on different dielectric substrates.

An indication of the amount of Ru needed to achieve film closure is obtained by combining SEM and TOFSIMS. A film which appears closed in SEM may still have small pinholes which are not observed due to the brightness of the metallic Ru film and the limited SEM resolution. SEM can therefore not be used to confirm at which amount of Ru film closure has been achieved. SEM can however be used to confirm that film closure has not yet been achieved when exposed substrate area can still be visually observed. SEM can therefore only provide a lower limit to the amount of Ru required

for film closure. TOFSIMS of the substrate Si ions on the other hand saturates at a stable background value for detected Si. When this background level is reached there is no more exposed substrate Si to be covered, and film closure is confirmed. However, because the escape depth for TOFSIMS exceeds the top surface if only slightly, the film closure point is likely reached before the substrate Si signal saturates at its background value. TOFSIMS therefore provides an upper limit for amount of Ru needed for film closure. Combining the results of SEM and TOFSIMS therefore provides a range in which the film closure point is situated.

Theoretical modeling

The formation of Ru nanoparticles during the early stages of Ru ALD on OSG is simulated using an adaptation of the mean-field (MF) model proposed by Grillo et al.[21,27] and by Kinetic Monte Carlo (KMC) simulations. A variety of possible growth mechanisms was considered and compared to the experimental data. An overview of the investigated models is presented in Table 1. These models are used to describe the evolution of the particle size distribution (PSD) of the Ru nanoparticles, the Ru areal density, and of the Ru surface coverage. Here, the term nanoparticle is used to denote clusters consisting of two or more atoms. These models in face assume irreversible nucleation/aggregation, that is, atoms cannot detach from clusters, irrespective of their size. This approximation provides a good description of the early stages of film growth at low temperatures (T<400 °C) and for metals characterized by a relatively high bond energy (E$_2$>1 eV), which is the case for the system at hand[35-37].

The MF model allows for: surface diffusion and irreversible aggregation of adatoms into nanoparticles; diffusion and coalescence of nanoparticles; and cyclic generation of adatoms on the substrate surface and on the surface of the nanoparticles. In addition, here we also consider that the growth of nanoparticles due to ALD surface reactions can take place only when a critical diameter (d_c) has been reached. In other words, we account for size-dependent nanoparticle growth due to ALD surface reactions. The beginning of each ALD cycle comprises the following steps:

- Instantaneous increase of the adatom density (at nm^{-2}) equal to G_s on the surface of the substrate that is not occupied by nanoparticles, that is the total substrate surface minus the nanoparticle coverage.

- Instantaneous growth of the nanoparticles > d_c such that the radial growth equals the steady-state growth-per-cycle of Ru ALD, that is ~0.03 nm/cycle (Figure S4).

Table 1: Overview of all growth models which were compared to experimental Ru growth data on OSG in this study

		G_s (10^{10} at/cm²cycle)	D_1 (nm²/cycle)	D_k (nm²/cycle)	d_c (nm)	Figure
(1)	NPs generated in 1st cycle, followed by cyclic deposition only on NPs[26]	0 (1.5 in 1st cycle)	0 (9000 in 1st cycle)	0 (D_1k^{-2} in 1st cycle)	0	S3
(2)	(1) + cyclic particle generation	1.5	0	0	0	S5
(3)	(2) + size-independent diffusion	1.5	*15*	D_1	0.4	S6
(4)	(3) + size-dependent growth	1.5	*10*	D_1	*0.85*	S7
(5)	(2) + size-dependent diffusion	1.5	*270*	$D_1k^{-8/3}$	0.4	S8
(6)	(5) + size-dependent growth	1.5	*270*	$D_1k^{-8/3}$	*0.85*	6

Model parameters in italics were fitted to best describe the experimental results, while all other values are either postulated (in case of D_1, D_k, and d_c) or measured (in case of G_s). For each growth model a comparison is made with experimental data, and this comparison can be found in the Figure denoted in the last column

During the rest of the cycle the surface species (i.e., adatoms and nanoparticles) aggregate due to surface diffusion. The diffusion rate of the surface species is assumed to follow the power law $D_k = D_1k^{-s}$ (nm²cycle⁻¹), where D_1 is the diffusion rate of adatoms, k is the number of atoms comprising the nanoparticle, and s is the mobility exponent[21,27]. Surface diffusion can take place during each stage of the ALD process and at varying rates depending on the reaction atmosphere. In fact, it might even be induced by the combustion reactions taking place during the second half-reaction[21,23,27]. Yet, lacking better insights into the details of the diffusion process and given that the experimental observables are obtained after the deposition process, here D_k is defined as an effective temporal average of the diffusion coefficient over a single cycle. The relation between the number of atoms k and the nanoparticle diameter d_k is estimated by approximating the Ru nanoparticles as hemispherical caps. The height-to-radius ratio of the nanoparticles was determined experimentally via AFM over a wide range of particle sizes, and was found to have a roughly constant value of to be 0.42±0.06 independent of particle size. This value holds for all islands measured on OSG, even though the broad PSD and varying cycle number allowed us to measure island radii which vary over more than an order of magnitude. The fraction of surface atoms of the Ru nanoparticles as a function of the size, that is the dispersion, was taken equal to the dispersion of a HCP truncated hexagonal bipyramid [1011]+[0001][38]. G_s was assumed to be constant with respect to the number of cycles and equal to the Ru areal density after 1 ALD cycle, which was estimated via TXRF to be 1.5·10¹⁰ Ru at/cm².

The MF model comprises of a set of rate equations that describes the evolution of the PSD by estimating the probability of binary collisions as a function of the mean density (nm⁻²) of all the surface species, hence the nomenclature mean-field. On the other hand, the KMC model describes the same physical picture by taking into account the collision of surface species via the lattice approximation. Each KMC simulation is constructed on a lattice consisting of 700x700 square sites, whose side is 0.3734 nm. The latter value is only an internal scaling reference that is used to relate the hopping frequency with D_k, and is thus not quantitatively related to actual number of surface sites that Ru atoms can occupy. During the course of one cycle, adatoms and nanoparticles occupy well-defined sites and can hop to neighboring sites with a frequency prescribed by the 2D diffusion coefficient $D_k = D_1k^{-s}$. Both adatoms and nanoparticles are described as circles. One adatom occupies one lattice site. The center of the circle corresponding to a nanoparticle also occupies one lattice site. The radius of the circle representing the nanoparticle corresponds to the projected radius of the hemispherical cap describing the nanoparticle as in the MF model. Thus, each nanoparticle also occupies all the sites whose area is either partially or completely covered by the circle representing the nanoparticle. When two or more surface species occupy the same site(s) these coalesce in a single nanoparticle comprising a number of atoms equal to the sum of the number of atoms comprising the coalescing entities.

The fitting parameters of both MF and KMC models are D_1, s, and d_c. To find the set of parameters that best describes the data we explored the following parameter space by means of the MF model: $[0.1\text{-}4.5\cdot10^4 \text{ nm}^2 \text{cycle}^{-1}]_{D_1} \times [0\text{-}8]_s \times [0.4\text{-}2.5 \text{ nm}]_{d_c}$. The latter was discretized in a 3D matrix 25x12x10 for a total of 3000 simulations.

It is worth noting that the extremes of the range of D_1 considered here correspond to a range of mean displacement of the adatoms of ~0.6-420 nm cycle⁻¹. The best fitting set was then used to run KMC simulations against which the MF model was validated.

The agreement between the simulations and experimental data was quantified in terms of the sum of squared errors of prediction (SSE):

$$SSE = \sum_{i=1}^{n}(y_i - f(x_i))^2$$

Where y_i is the experimental observable, that is the probability density function (PDF) for the PSD, the nanoparticle number density (ND), the Ru areal density (L), or the coverage (C%), and $f(x_i)$ is the predicted observable as a function of the variable x_i, which is either the diameter for the PDF at a given cycle or the number of cycles for the other

observables. We then defined the error with respect to the PSD, the ND, the L, and the $C\%$ as follows:

$$Err_{PSDs} = \sum_{j} \frac{SSE_{PSDs}^{j}}{\langle PDF \rangle_{j}^{2}}; Err_{ND} = \frac{SSE_{ND}}{\langle ND \rangle^{2}};$$

$$Err_{L} = \frac{SSE_{L}}{\langle L \rangle^{2}}; \; Err_{C\%} = \frac{SSE_{C\%}}{\langle C\% \rangle^{2}}$$

where j is the number of cycles. In particular, the error with respect to the PSD was defined as the sum of the SSEs at different cycles weighted by the respective mean squared PDF. By doing so, each experimental PSD has about the same weight in the estimation of the agreement. The overall agreement was evaluated by considering the normalized sum of the errors with respect to the PSDs, ND, and L:

$$Norm.\; Err. = \frac{Err_{PSDs}}{max\{Err_{PSDs}\}} + \frac{Err_{ND}}{max\{Err_{ND}\}} + \frac{Err_{L}}{max\{Err_{L}\}}$$

$Err_{C\%}$ was not taken into account as $SSE_{C\%}$ is correlated with SSE_{ND} and SSE_{PSDs}. The normalized error thus defined is a number that ranges between 0 and 3.

Results and discussion

Surface properties of the dielectric layers

The surface properties of each dielectric substrate have been characterized prior to Ru ALD using a combination of Water CA, ATR-FTIR, and surface -OH group quantification. The surface density of -OH groups was determined because a variety of ALD precursors have been shown to react readily with surface -OH groups, e.g. trimethylaluminium (TMA), HfCl$_4$, and 2,4-(dimethylpentadienyl)-(ethylcyclopentadienyl)Ru [(DMPD)(EtCpRu)][1,39-41]. An overview of the dielectric surface properties is presented in Table 2.

Al$_2$O$_3$, HfO$_2$, and PEALD SiO$_2$ are primarily -OH terminated, while the thermally grown SiO$_2$ surface is Si-O-Si terminated. The high surface -OH density of the ALD-deposited Al$_2$O$_3$ and HfO$_2$ films is well established in literature[3,42,43]. The PEALD SiO$_2$ also shows a high surface –OH density of 2.5 ± 0.1 -OH/nm^2, and the hydrophilicity of this surface is evidenced by a low water CA of 17°. On the other hand, thermally grown SiO$_2$ displays a lower surface density of -OH groups (0.42 ± 0.06) -OH/nm^2. This is expected for dry thermal SiO$_2$ grown at 1000°C with O$_2$ as an oxidizer, as surface -OH groups are likely to condense to siloxane bridges at high temperature (2SiOH $\rightarrow$ Si-O-Si + H$_2$O)[44]. The observed surface -OH density is in agreement with values of 0.3-0.4 -OH/nm^2 reported in literature[34]. The lower surface -OH density for the dry thermal SiO$_2$ as compared to the PEALD SiO$_2$ results in a lower surface energy, which is confirmed by a higher water CA on the dry thermal SiO$_2$ (38°). PEALD SiO$_2$ will therefore from now on be referred to as hydrophilic SiO$_2$, while dry thermal SiO$_2$ will be referred to as hydrophobic SiO$_2$.

The surface of the OSG film is primarily Si-CH$_3$ terminated as evidenced by water CA and ATR-FTIR. OSG is the most hydrophobic surface investigated in this study, with a water CA of 103°. A high water CA value can be expected for the surface of OSG films, which typically consists of hydrophobic surface groups such as Si-H and/or Si-alkyl groups[45]. Furthermore, no surface -OH groups were detected as after HfCl$_4$ exposure the Hf- coverage was below the detection limit of RBS. The chemical nature of the groups present in and on top of the OSG layer is further investigated by ATR-FTIR, showing the presence of a Si-O-Si network as well as Si-CH$_3$ groups in and on top of the layer (Figure 1). The Si-O-Si network can be identified by characteristic antisymmetric stretch modes at 1135 cm^{-1} and 1063 cm^{-1}. CH$_3$-related peaks can be identified at 2969 cm^{-1} (CH$_3$ antisymmetric stretching), 1412 cm^{-1} (CH$_3$ antisymmetric bending), and 1273 cm^{-1} (CH$_3$ symmetric bending)[46]. Chemical bonding between these CH$_3$ groups and silicon is confirmed by Si-C stretches observed at 802 cm^{-1} and 773 cm^{-1}.

Table 2: Surface properties and their impact on Ru particle formation for the dielectric substrates investigated in this study.

Surface	Water CA (°)	Surface -OH/nm^2	Ru nanoparticle density (10^{12} cm^{-2}) for $4 \cdot 10^{15}$ at/cm^2 Ru
Al$_2$O$_3$	15 ± 2	6[42]	
HfO$_2$	12 ± 1	2.8[43]	
PEALD SiO$_2$	17 ± 1	2.5 ± 0.1	2.7
Dry thermal SiO$_2$	38 ± 2	0.42 ± 0.06	1.0
Dry thermal SiO$_2$ + 1 H$_2$O pulse (325°C)	34 ± 1		
OSG	103 ± 1	< 0.1	0.20
OSG + 100 O$_2$ pulses (325°C)	104 ± 1		
OSG + 100 H$_2$O pulses (325°C)	103 ± 0		

Surface -OH group density is determined by HfCl$_4$ exposure and subsequent Hf RBS as described in experimental methods. For PEALD SiO$_2$, Dry thermal SiO$_2$, and OSG the Ru nanoparticle density corresponding to $4 \cdot 10^{15}$ at/cm^2 Ru is shown as obtained by SEM

No O-H stretch modes are detected in the 2500-3700 cm^{-1} range, no Si-H stretch modes are detected in the 2300-2000 cm^{-1} range[47], and no peaks related to organic groups other than CH$_3$ could be identified from ATR-FTIR. Recalling the high water CA of 103° indicates that the surface is mainly Si-CH$_3$ terminated rather than Si-O-Si terminated (compare water CA of 38° for Si-O-Si terminated hydrophobic SiO$_2$). We conclude that the OSG film is primarily composed of a Si-O-Si network and Si-CH$_3$ groups, and that the surface is mostly Si-CH$_3$ terminated.
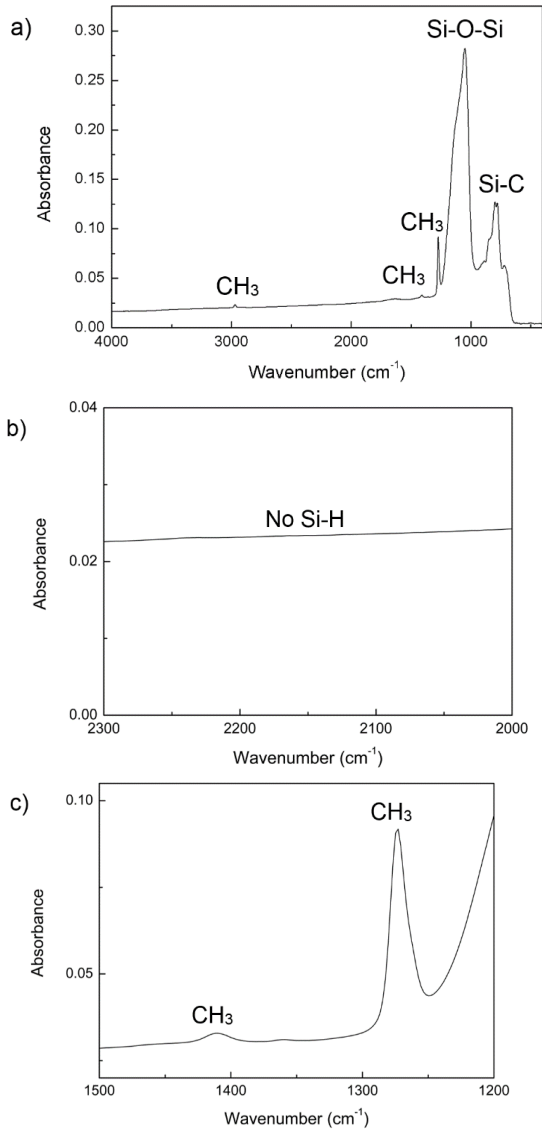

Figure 1: OSG contains primarily Si-CH$_3$ and Si-O-Si bonds as shown by ATR-FTIR. a) ATR-FTIR spectrum of 100nm OSG on Si (100) b) 2300-2000 cm^{-1} region characteristic of the Si-H stretch c) 1500-1200 cm^{-1} region characteristic for CH$_3$ bending modes

Impact of dielectric surface on Ru ALD growth evolution

This section discusses how different dielectric surface terminations affect the amount of deposited Ru during the initial growth regime. The Ru ALD shows surface-dependent growth inhibition on dielectric surfaces. This is illustrated by the growth curves in Figure 2, where the amount of deposited Ru is followed as a function of ALD cycle number.
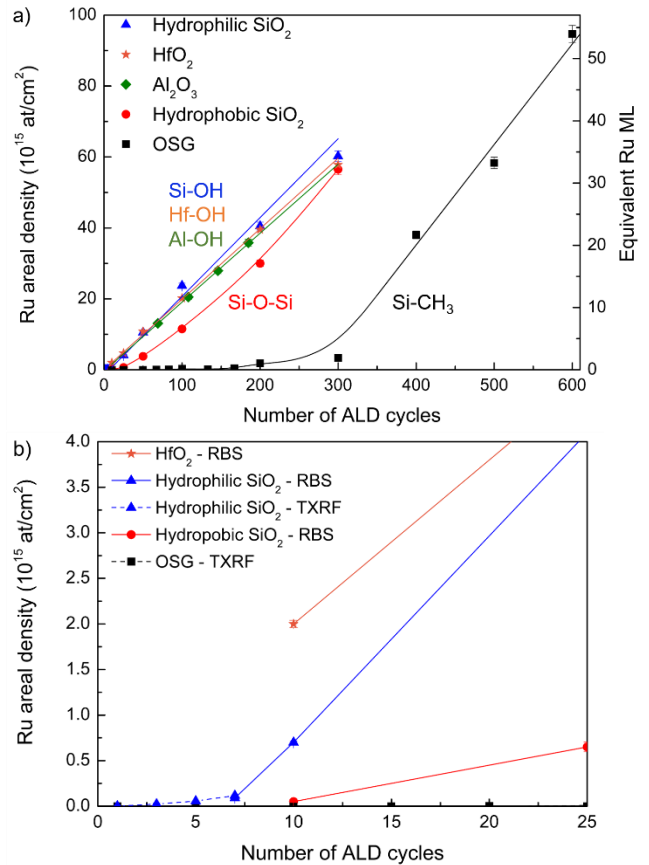

Figure 2: Dielectric surface termination affects Ru growth inhibition. a) Ru coverage measured by RBS for increasing ALD cycle number on hydrophilic SiO$_2$, HfO$_2$, Al$_2$O$_3$, hydrophobic SiO$_2$, and OSG, b) inset for low ALD cycle number, showing Ru RBS and TXRF for the initial ALD cycles. Lines are provided as a guide to the eye

Linear growth occurs immediately on the HfO$_2$ and Al$_2$O$_3$ surfaces (Figure 2). These surfaces exhibit a high surface -OH density within the 2.5 – 6 -OH/nm^2 range (Table 2), suggesting that surface -OH groups facilitate EBECHRu chemisorption. Linear growth on an -OH terminated surface has been previously reported for EBECHRu/O$_2$ ALD on plasma-treated SiCN[48].

In contrast, on hydrophilic SiO$_2$ we observe a short ~7 cycles inhibition period where no Ru is detected by RBS, while the surface -OH density is comparable to that of HfO$_2$ (2.5 and 2.8 -OH/nm^2 respectively). This suggests that the precursor is less reactive towards Si-OH groups as compared to the more polar -OH bonds like Hf-OH. This is confirmed by TXRF measurements which show that the growth-per-cycle (GPC) during the initial cycles stays below 0.03·10^{15} Ru at/cm^{2}cycle on hydrophilic SiO$_2$ (Figure 2b). Moreover, the Ru areal density deposited in the first ALD cycle equals 1.5·10^{12} Ru at/cm^2 which is two orders of magnitude lower

than the -OH areal density ($2.5 \cdot 10^{14}$ -OH/cm^2). This suggests that only a small fraction of all Si-OH groups reacts with the EBECHRu precursor during the first cycle. The precise nature of the interaction between the EBECHRu precursor and surface -OH groups is currently not yet understood. After the short inhibition period, the Ru GPC rapidly progresses into the linear regime. The observed GPC in the linear regime equals $0.2 \cdot 10^{15}$ Ru at/cm^{2}cycle or 0.03 nm/cycle, which is the same as the steady-state GPC previously reported for EBECHRu/O$_2$ ALD on SiO$_2$[20].

On the hydrophobic SiO$_2$ surface, a longer inhibition period is observed. After 25 cycles, only $(0.65 \pm 0.05) \cdot 10^{15}$ Ru at/cm^2 has been deposited corresponding to less than half of a monolayer (ML) equivalent of Ru (using bulk Ru atomic density of $7.36 \cdot 10^{22}$ at/cm^3 [49]). This is much lower compared to the $(4.1 \pm 0.2) \cdot 10^{15}$ Ru at/cm^2 or 2.3 ML equivalent observed on hydrophilic SiO$_2$ for the same amount of cycles. The longer inhibition on hydrophobic SiO$_2$ suggests that Ru ALD proceeds slower on siloxane bridges than on -OH groups. Alternatively, the siloxane bridges could be slowly hydrolyzed by H$_2$O at 325°C (Si-O-Si + H$_2$O → 2Si-OH[44]), as H$_2$O is a reaction product of the combustion reactions that occur during the EBECHRu and O$_2$ half-cycles[20]. These newly formed Si-OH groups may act as chemisorption sites in subsequent ALD cycles. The exposure of hydrophobic SiO$_2$ to a single 0.4s H$_2$O pulse at 325°C indeed decreases the Water CA from 38±2° to 34±1° (Table 2), which supports surface modification by hydrolysis. Between 25 and 300 cycles, the Ru GPC increases up to $0.3 \cdot 10^{15}$ at/cm^{2}cycle, which is higher than the steady GPC ($0.2 \cdot 10^{15}$ at/cm^{2}cycle). This temporary growth rate enhancement after inhibition is frequently observed in ALD, and may be related to particle-type growth behavior due to increased surface roughness[26]. The steady GPC is reached after 300 cycles, with $56.5 \cdot 10^{15}$ Ru at/cm^2 deposited, the equivalent of 32 Ru ML.

The longest inhibition period among the investigated dielectrics is observed on the OSG surface. No Ru is detected by RBS during the first 50 cycles and only $(0.29 \pm 0.1) \cdot 10^{15}$ Ru at/cm^2 is detected after 100 ALD cycles, corresponding to less than 1 ML equivalent of Ru. TXRF predicts a Ru deposition of $1.5 \cdot 10^{10}$ Ru/cm^2 during the first cycle, which is two orders of magnitude below the initial deposition on hydrophilic SiO$_2$. After this long inhibition period, the amount of Ru increases rapidly between 300-400 cycles to $0.35 \cdot 10^{15}$ at/cm^{2}cycle, almost two times higher than the steady-state GPC ($0.2 \cdot 10^{15}$ at/cm^{2}cycle). The steady-state linear GPC is only observed after deposition of $(38 \pm 1.1) \cdot 10^{15}$ Ru at/cm^2,

equivalent to 22ML of Ru. The long inhibition period and low initial rate of Ru deposition indicate the weak interaction between the ALD precursors and the OSG surface. The initial Ru deposition is expected to originate from thermal precursor decomposition as previously characterized for EBECHRu/O$_2$ ALD[19,20]. Alternatively, the initial chemisorption could occur on defect sites at the surface given the low areal density of $1.5 \cdot 10^{10}$ Ru/cm^2 in the first ALD cycle. As discussed above, the OSG surface is primarily populated with Si-CH$_3$ groups. We conclude that the reactivity of EBECHRu and O$_2$ with surface Si-CH$_3$ groups is low at 325°C, as only weak van der Waals interactions are expected between Si-CH$_3$ and the Ru precursor ligands as proposed for 2,4-(dimethylpentadienyl)-(ethylcyclopentadienyl)Ru. These interactions are however not expected to play a significant role at the high deposition temperature of 325°C[41]. In addition, the Si-CH$_3$ groups remain stable during O$_2$ and H$_2$O exposure at 325°C: the OSG surface was exposed to a series of 100 O$_2$ pulses or 100 H$_2$O pulses (H$_2$O is a product of the ALD combustion reaction) in order to determine whether these reagents could affect the OSG surface termination. Neither O$_2$ nor H$_2$O exposures resulted in significant changes in the water contact angle (Table 2). The initial Ru adsorption could therefore be attributed to the slow thermal decomposition of the EBECHRu precursor. Indeed, noble metal ALD processes which are inhibited on dielectrics can grow slowly through random precursor decomposition leading to deposition of metal, which eventually catalyzes coreagent decomposition for further growth[16]. These findings corroborate that Ru ALD on the OSG surface is governed either by a slow precursor decomposition process in the gas phase or on the unreactive Si-CH$_3$ sites, or by adsorption on a low areal density of surface defect sites.

Nanoparticle growth on different dielectric surfaces

Next, we investigate how different starting surfaces affect the Ru morphology and nanoparticle formation behavior. We focus on the differences between the hydrophilic SiO$_2$, hydrophobic SiO$_2$, and OSG substrates. The morphology of the Ru deposition was examined at an equal Ru areal density of $4 \cdot 10^{15}$ at/cm^2 (2.3 ML equivalent) for the hydrophilic SiO$_2$, hydrophobic SiO$_2$, and OSG surfaces (SEM, Figure 3). The particle density and the initial surface -OH density are reported in Table 2 and the corresponding particle size distributions are shown in Figure 4. On all surfaces, we observe the arrangement of Ru in particles (Figure 3 and 4) rather than as a continuous film, confirming an island-type growth mode.
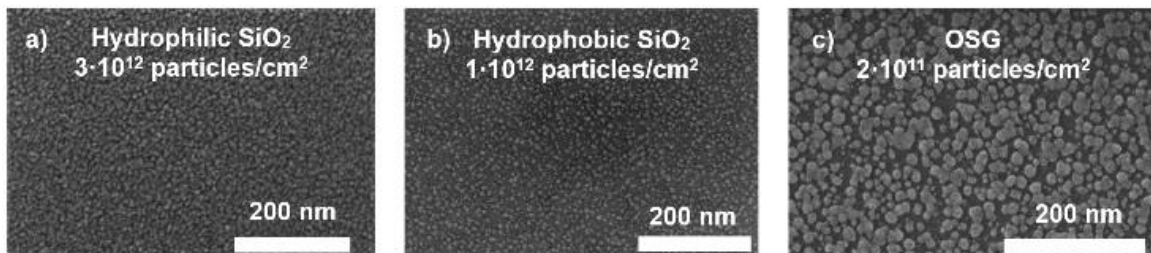

Figure 3: Surface-dependent Ru particle formation is illustrated by SEM. Images shown for Ru ALD on a) 25 cycles on hydrophilic SiO$_2$, b) 50 cycles on hydrophobic SiO$_2$, and c) 300 cycles on OSG. The Ru areal density is equal to $4 \cdot 10^{15}$ at/cm^2 in all cases.
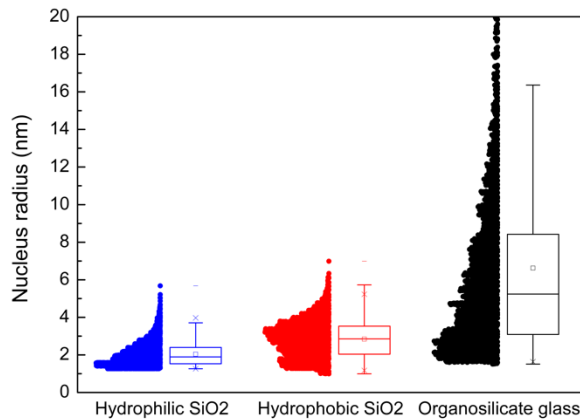
Figure 4: Normalized particle size distributions corresponding to $4 \cdot 10^{15}$ at/cm^2 for different dielectric surfaces (25 Ru ALD cycles on hydrophilic SiO$_2$, 50 Ru ALD cycles on hydrophobic SiO$_2$, 300 Ru ALD cycles on OSG). Outliers with radii larger than 20nm have been omitted.

On hydrophilic SiO$_2$, SEM shows the existence of Ru particles even though the amount of Ru increases almost linearly with cycle number (Figure 2 and 3). The particles have an average radius of 2 nm, while a radius of 0.75 nm would be expected according to the growth model by Puurunen and Vandervorst, which assumes layer-by-layer growth from fixed initial defect sites by chemisorption (according to this model 0.03nm/cycle for 25 cycles gives a radius of 0.75 nm)[26]. In addition, the particle density ($2.7 \cdot 10^{12}$ cm^{-2}) is one order of magnitude lower than the Ru GPC in all but the first ALD cycle (0.01-0.2 $\cdot 10^{15}$ cm^{-2}cycle^{-1}). These two observations confirm the importance of surface diffusion in the growth process. It has indeed been reported that the formation and growth of metal nanoparticles (Cu, Pt) by ALD is dictated not only by chemisorption, but also by surface diffusion of adatoms, nanoparticle formation, diffusion and coalescence, and atom attachment and detachment from nanoparticles[21,22]. Similarly to Cu and Pt, Ru has a high surface energy compared to SiO$_2$ (3.05 J/m^2 vs 0.0518 J/m^2 [24,25]) and is therefore expected to undergo aggregation, especially considering the relatively high deposition temperature of 325°C.

A diffusion-mediated growth mechanism can also be proposed for Ru ALD on the hydrophobic SiO$_2$ and OSG surfaces, where the particle densities are even lower and the average particle size is larger for the same Ru areal density (Figure 3 and 4). On hydrophobic SiO$_2$, the particle density is $1.0 \cdot 10^{12}$ cm^{-2} which is slightly lower as compared to hydrophilic SiO$_2$ ($2.7 \cdot 10^{12}$ cm^{-2}, Table 2). The lower particle density could be attributed to increased surface diffusion on the hydrophobic surface, as the higher hydrophobicity indicates a lower surface energy of the hydrophobic SiO$_2$ substrate compared to hydrophilic SiO$_2$. This in turn provides a larger driving force for aggregation of the deposited Ru on hydrophobic SiO$_2$. Additionally, a lower -OH density of $4.2 \cdot 10^{13}$ cm^{-2} may result in a lower EBECHRu adsorption rate during the initial cycles compared to hydrophilic SiO$_2$, explaining the inhibition period. As a result, more cycles are required to reach the Ru coverage of $4 \cdot 10^{15}$ at/cm^2, yielding

a lower density of larger particles (average radius of 2.9nm for hydrophobic SiO$_2$ vs 2nm for hydrophilic SiO$_2$, Figure 4).

On the OSG surface, a much lower particle density of $2 \cdot 10^{11}$ cm^{-2} is observed (Figure 3). The Ru particle size distribution on OSG is more polydisperse compared to the SiO$_2$ surfaces (Figure 3, 4, and 6): the standard deviation is 79% of the average value, compared to 31% for hydrophilic and 34% for hydrophobic SiO$_2$. The full interquartile range of the particle size distribution has a radius below 9nm, which is the expected size obtained in 300 ALD cycles based on steady-state growth of the Ru particles (0.03nm/cycle). This indicates that on OSG, either most particles have been generated well after the first ALD cycle which can be attributed to the significantly lower precursor chemisorption, or particles grow slower compared to the steady-state outward Ru particle GPC. The growth mechanism on OSG will be studied in greater detail in the combined modeling/experimental section further in this work.

Ru layer closure on different dielectric surfaces

Next, we study the Ru film closure on hydrophilic SiO$_2$, hydrophobic SiO$_2$, and OSG surfaces. The closure of the Ru film marks the end of the surface-dependent growth regime. After the film closure, the influence of the substrate may disappear or only be indirectly apparent, e.g. through differences in crystallinity and/or roughness of the grown film. When the precursor reacts readily with the substrate surface either a 2D-like growth regime or an island-growth regime characterized by a high density of nanoparticles are typically observed. Both regimes lead to a rapid film closure compared to substrate that exhibit poor reactivity towards the precursor[26]. As TOFSIMS is a technique sensitive to the topmost surface, it can be applied to assess film closure as described in the experimental details. Figure 5 shows how the TOFSIMS ^{30}Si$^+$ ion intensity decays with increasing amounts of deposited Ru on hydrophilic SiO$_2$, hydrophobic SiO$_2$, and OSG. The film closure point falls within a range of Ru areal density which can be determined by combining SEM and TOFSIMS (see experimental methods).

Ru ALD on hydrophilic SiO$_2$ shows faster film closure compared to hydrophobic SiO$_2$ and OSG (Figure 5). The Ru deposition proceeds by a particle-type growth mode even on hydrophilic SiO$_2$, explaining why film closure only occurs after the deposition of the equivalent of 6-9 Ru MLs. On hydrophobic SiO$_2$ and OSG the film closes occurs much later: after the deposition of the equivalent of 17-32 and 22-33 Ru MLs, respectively. The fact that the film closure is reached on both hydrophobic SiO$_2$ and OSG after the deposition of about the same amount of Ru is unexpected because the growth on OSG is characterized by a lower density of large nanoparticles. Yet, the differences between closure points on both surfaces may be in fact obscured by the experimental range covered here (17-33 ML equivalent). Nonetheless, this illustrates how changes in the surface chemistry of SiO$_2$ can significantly impact the film closure speed and therefore the film morphology. Effectively, the low precursor reactivity towards Si-O-Si and Si-CH$_3$ terminated surfaces results in low particle densities (Figure 3) and thus in large interparticle distances compared to Ru ALD on Si-OH terminated SiO$_2$. Low particle densities translate into a film

closure characterized by the coalescence of large nanoparticles, and thus into rough films.
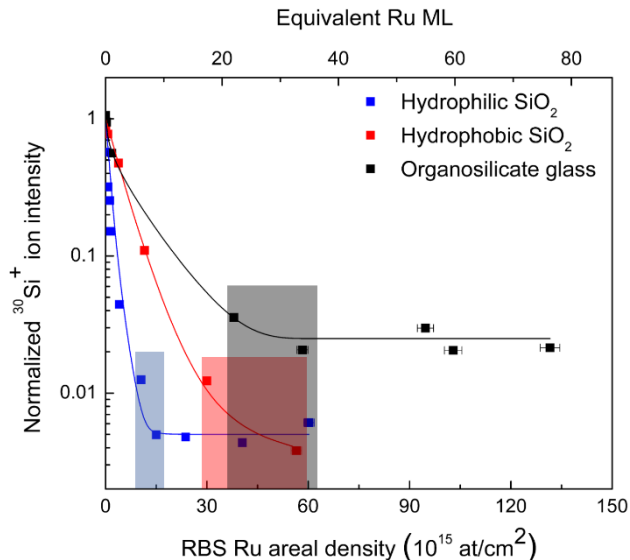

Figure 5: Ru film closure is achieved more rapidly for hydrophilic SiO₂ compared to less reactive dielectric surfaces. TOFSIMS $^{30}Si^+$ intensity is shown for increasing amount of Ru deposited on hydrophilic SiO₂, hydrophobic SiO₂, and OSG to determine the film closure point as described in experimental methods. The shaded areas indicate the range of deposited Ru in which the film closure point is situated on each substrate. The difference in saturation values between SiO₂ and OSG originates from the low initial areal Si density on OSG as compared to SiO₂.

Modeling the early stages of growth on OSG

To gain insight into the processes governing the early stages of Ru ALD on OSG, we described the growth of Ru nanoparticles during the low coverage regime via mean-field (MF) and Kinetic Monte Carlo (KMC) models in a variety of possible growth scenarios (Table 1). OSG was selected as a substrate for this study as the film closure is slowest amongst the investigated substrates, providing us with the longest process window for studying growth on the starting substrate (Figure 2 and 5). The MF model used here is an adaptation of the model already described in previous works[21,27]. This model takes into account the cyclic deposition of adatoms arising from ALD surface reactions and their aggregation into nanoparticles via surface diffusion and coalescence. The KMC model describes the same physical processes as the MF model and is used as a validation tool (see methods section).

Unlike previous formulations of the model, here we also take into account the possibility that the nanoparticles can grow via size-dependent ALD surface reactions. As described in the introduction, the catalytic activity of Ru nanoparticles towards oxygen dissociation is known to depend strongly on their size. Here, we account for size-dependent reactivity by assuming that the Ru nanoparticles start to grow due to ALD surface reactions only when they have reached a critical diameter (d_c).

Both MF and KMC models have three parameters: the average diffusion rate of adatoms during each ALD cycle D_1, the mobility exponent s, which determines how the mobility of the nanoparticles scales with their size, and the critical diameter d_c. To determine the set of parameters that best describes the nanoparticle growth we relied on the MF model. We evaluated the agreement between predicted and experimental particle size distributions (PSDs) for various ALD cycle numbers, the Ru areal density, the nanoparticle number density and the surface coverage by varying D_1, s, and d_c within the parameter space $[0.1\text{-}4.5\cdot10^4 \text{ nm}^2 \text{ cycle}^{-1}]_{D_I}\times[0\text{-}8]_s\times[0.4\text{-}2.5 \text{ nm}]_{d_c}$ (Figure S1). The best fitting set of parameters was then used to run KMC simulations for validation (Figure 6b-f).

The experimental PSDs are broad and characterized by a tail that shifts towards the large-size side with increasing number of cycles (Figure 6c). The coverage, the Ru areal density, and the nanoparticle number density all increase rapidly with increasing number of cycles (Figure 6d-f). Trivially, growth scenarios where deposition on the substrate and surface diffusion are suppressed after the first cycle ($G_s = D_k = 0$), such as the one proposed by Puurunen and Vandervorst, cannot account for the experimental observations (Figure S3)[26]. In such scenarios the PSD would remain narrow with increasing number of cycles while shifting towards the large-size side. Furthermore, the nanoparticle number density would remain constant, which is clearly not the case here. Another trivial scenario is the one in which surface diffusion is suppressed and deposition takes place both on the substrate and on the existing adatoms and nanoparticles. This also cannot account for the experimental observations (Figure S5). In that case, the coverage, the Ru areal density, and the NP number density would increase rapidly. We estimate that the coverage would be as high as ~40% after 167 cycles, as opposed to the 3% observed experimentally. A coverage of 40% translates into an average distance between surface species that is on the order of the atomic spacing. At such distances neglecting the role of surface diffusion and nanoparticle coalescence is certainly a poor approximation, especially considering the high surface energy of Ru and the relatively high deposition temperatures (325°C). Furthermore, this scenario, while producing broad PSDs, still fails to account for the long tail on the large-size side.

Number of Cycles

| 67 | 83 | 100 | 133 | 167 |

SEM Micrographs

a.

KMC Simulations

b.

○ **Experiments** Vs ●— **MF Model &** ◇— **KMC Model**
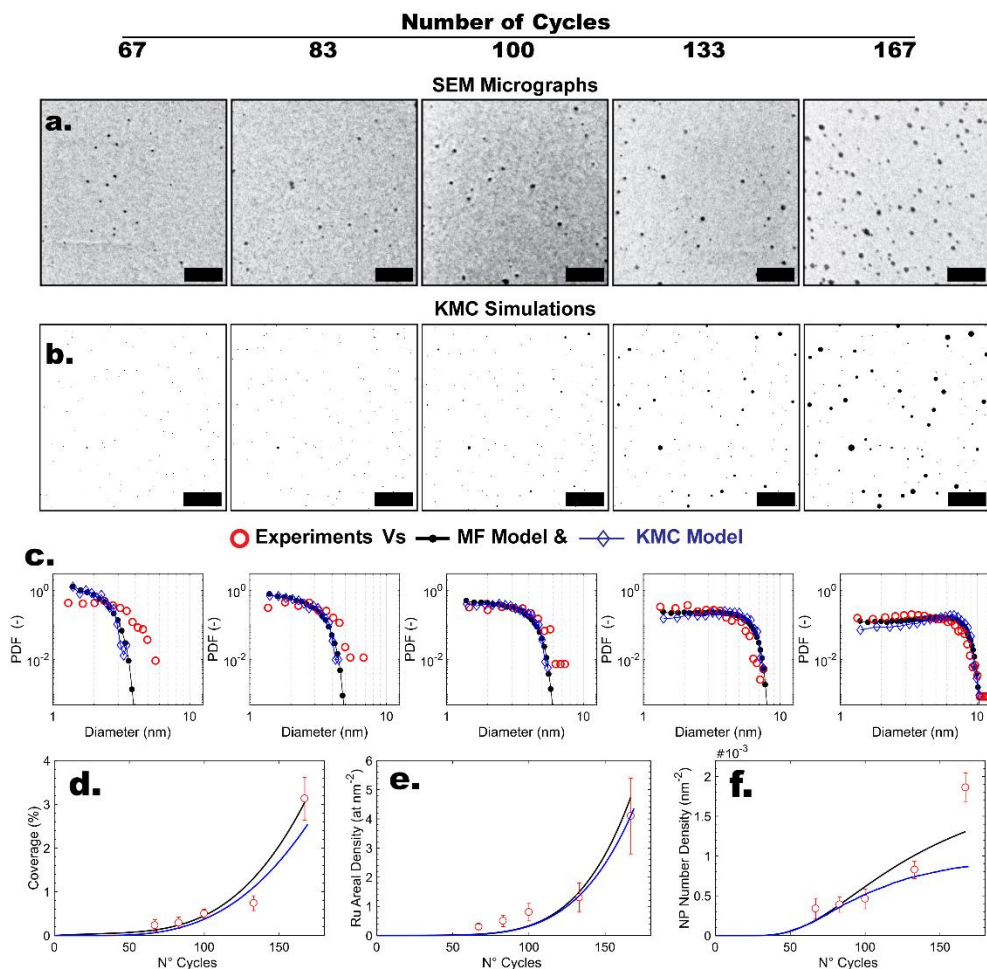
c.

d.　　　e.　　　f.

Figure 6: Early stages of Ru ALD on OSG as investigated experimentally and through mean-field and Kinetic Monte Carlo (KMC) simulations. (a) Representative scanning electron microscopy (SEM) micrographs of Ru nanoparticles deposited after 67, 83, 100, 133, and 167 ALD cycles (During the first 25 cycles no particles are large enough to be detected by SEM). The SEM micrographs were modified by inverting the color and optimizing the contrast to improve the visibility of the nanoparticles. The scale bar indicates 50 nm in each case. (b) KMC simulations of Ru ALD obtained by letting $D_k = D_1 k^{-8/3}$, where $D_1 = 270$ nm^{2}s^{-1}, and the radial growth-per-cycle of the nanoparticles equal to 0.03 nm cycle^{-1} for nanoparticles that have reached a critical diameter (dc) of 0.85 nm. (c) Particle size distributions expressed in terms of probability density function (PDF) of the Ru nanoparticles obtained after 67, 83, 100, 133, and 167 ALD cycles as obtained via image analysis of SEM micrographs and mean-field and KMC simulations using the same parameters as in (b). Evolution of the coverage (d), the Ru areal density (e), and the nanoparticle number density (f) as obtained experimentally and via mean-field and KMC simulations. With the exception of the Ru areal density, nanoparticles with a diameter < 1.4 where not taken into account in the estimation of both simulated and experimental observables, since such nanoparticles were below the detection limit of the SEM analysis. The results regarding the KMC simulations were obtained by running 40 simulations constructed on a 700x700 lattice.

The experimental observations are best described when accounting for adsorption on the substrate, surface diffusion and aggregation of single atoms and nanoparticles, and size-dependent direct growth of existing nanoparticles due to surface reactions on the nanoparticles (Figure 6 and Figure S1 as well as Figure S6 to S8). In particular, the agreement between simulations and experimental data is best when the critical diameter d_C is ∼0.85 nm and the mobility exponent s is > 1 (Figure S1). In other words, the nanoparticles initially grow only by means of diffusion and aggregation, and direct deposition on nanoparticles starts to occur only when they have reached critical size. This result is consistent with the notion that catalytic decomposition of the

ligands by oxygen requires a minimum Ru particle size. These results also explain the long inhibition period, as Ru deposition initially proceeds only through very slow precursor chemisorption on the substrate followed by diffusion of adatoms, while direct deposition on the particles only proceeds once the few initial adatoms have coalesced into particles of critical size.

A mobility exponent >1 suggests that the diffusion and coalescence of large nanoparticles plays a minor role. This is not surprising as the mean center-to-center distance between surface species goes from ∼80 nm to ∼20 nm in the cycle range 1-167. Such distances make the meeting of two

large nanoparticles an unlikely event, while fast-diffusing atoms and small nanoparticles can still meet and aggregate. Nonetheless, the coalescence of large neighboring nanoparticles that grow while being immobile can still take place and accounts for the long tail on the large-size side in the PSD (see also the KMC video in the Supporting Information).

As already argued in our previous work[27], ALD of nanoparticles is often characterized by an exponential increase in the amount of material being deposited, provided that: the deposition process takes place on both the substrate and the nanoparticles, and that the GPC on the ALD-grown material is higher than on the substrate. This is the case for ALD of noble metals, where the ALD reactions on certain substrates can even be completely suppressed, enabling area selective deposition[16]. In fact, if we assume that the amount of Ru deposited per cycle on OSG stays constant throughout the ALD experiment, this would account for only $\sim 2.5 \cdot 10^{12}$ Ru at/cm^2 of the $\sim 4 \cdot 10^{14}$ Ru at/cm^2 found after 167 cycles. In other words, almost the totality of the Ru deposited after 167 cycles arises from Ru deposited directly onto Ru nanoparticles. Because the direct deposition on nanoparticles only occurs once particles of critical size have been formed by diffusion and coalescence, the initial growth process is almost completely governed by the surface-dependent initial precursor chemisorption and metal diffusion rates.

Conclusion

The aim of this work was to determine the surface dependence and growth mechanism of EBECHRu/O$_2$ ALD on dielectric substrates. The nature of the dielectric surface strongly affects both the precursor chemisorption and the film morphology. EBECHRu chemisorption occurs most rapidly on surface -OH groups, followed by Si-O-Si bridges, while adsorption on Si-CH$_3$ groups is extremely slow. Nanoparticles form on both SiO$_2$ and OSG surfaces, and their growth is governed by diffusion and coalescence. This phenomenon is driven by the minimization of surface energy, which constitutes a particularly strong driving force for noble metals on dielectric surfaces. While diffusion-mediated growth occurs on all the surfaces considered here, at a given amount of deposited Ru, less reactive surfaces display lower particle densities. Mean-field and Kinetic Monte Carlo modeling of our experiments show that the initial stages of Ru ALD on OSG are best described when accounting for (i) cyclic generation of nanoparticles, (ii) size-dependent nanoparticle diffusion, and (iii) size-dependent nanoparticle reactivity. In particular, our models suggest that the nanoparticles start growing due to ALD reactions on their surface only after they reach a critical size. This is consistent with the well-known size-dependent catalytic activity of Ru nanoparticles towards O$_2$ decomposition. Although this phenomenon is well-known to the catalysis community, so far its impact on the initial stages of ALD processes based on combustion reactions has never been described in quantitative terms. We expect that the growth model described here for Ru ALD might also be applicable to ALD of other noble metals on poorly reacting substrates.

Furthermore, on one hand, the diffusion-mediated growth behavior of Ru ALD on dielectrics explains the difficulties reported in achieving smooth ultra-thin Ru films. On the other hand, the understanding of the importance of surface diffusion might also inform the design of deposition processes for dispersed nanoparticles of well-defined size, such as is required in catalysis. Surface diffusion might also affect area-selective processes where growth and non-growth pattern are in close proximity. This work has investigated the growth mechanism of EBECHRu/O$_2$ ALD on dielectric substrates, yet the precise surface reactions between various precursors and substrates remain beyond the scope of the current work. Combining this insight into the initial growth mechanism with atomistic insight into surface reactions could reveal a more complete physicochemical picture of the initial stages of ALD growth.

SUPPORTING INFORMATION

Evaluation of the agreement between experimental observables and the values predicted by the model for Ru ALD on OSG. Correlations between SSE predictions of experimental variables used in the MF model. MF simulations for Ru ALD on OSG using different sets of assumptions and their comparison to the observed growth behavior. KMC video illustrating the Ru growth evolution on OSG.

AUTHOR INFORMATION

Corresponding Author

* Job.Soethoudt@imec.be
* f.grillo@tudelft.nl

Present Addresses

† ASM Belgium, Kapeldreef 75, 3001, Leuven, Belgium

REFERENCES

[1]George, S. M. Atomic Layer Deposition: An Overview, *Chem. Rev.* **2010**, *110*, 111-131.

[2]Knapas, K.; Ritala, M. *In Situ* Studies on Reaction Mechanisms in Atomic Layer Deposition, *CRC Cr. Rev. Sol. State* **2013**, *38*, 167-202.

[3]Puurunen, R. L. Surface chemistry of atomic layer deposition: A case study for the trimethylaluminum/water process, *J. App. Phys.* **2005**, *97*, 121301.

[4]Mackus, A. J. M.; Verheijen, M. A.; Leick, N.; Bol, A. A.; Kessels, W. M. M. Influence of Oxygen Exposure on the Nucleation of Platinum Atomic Layer Deposition: Consequences for Film Growth, Nanopatterning, and Nanoparticle Synthesis, *Chem. Mater.* **2013**, *25*, 1905-1911.

[5]Mackus, A. J. M.; Bol, A. A.; Kessels, W. M. M. The use of atomic layer deposition in advanced nanopatterning. *Nanoscale* **2014**, *6(19)*, 10941-10960.

[6]Van Bui, H.; Grillo, F.; Van Ommen, J. R. Atomic and molecular layer deposition: off the beaten track. *Chem. Commun.* **2017**, *53*, 45-71.

[7]Christensen, S. T.; Feng, H.; Libera, J. L.; Guo, N.; Miller, J. T.; Stair, P. C.; Elam, J. W. Supported Ru–Pt bimetallic nanoparticle catalysts prepared by atomic layer deposition. *Nano Lett.* **2010**, *10(8)*, 3047-3051.

[8]Wen, L. G.; Adelmann, C.; Pedreira, O. V.; Dutta, S.; Popovici, M.; Briggs, B.; Heylen, N.; Vanstreels, K.; Wilson, C. J.; Van Elshocht, S.; Croes, K.; Bömmels, J.; Tőkei, Z. Ruthenium metallization for ad-

vanced interconnects. Paper presented at the Interconnect Technology Conference / Advanced Metallization Conference, San Jose, CA, May 23-26 **2016**. doi: 10.1109/IITC-AMC.2016.7507651

[9]Kang, J.; Zhang, S.; Zhang, Q.; Wang, Y. Ruthenium nanoparticles supported on carbon nanotubes as efficient catalysts for selective conversion of synthesis gas to diesel fuel. *Angew. Chem. Int. Ed.* **2009**, *121(14)*, 2603-2606.

[10]Joo, S. H.; Park, J. Y.; Renzas, J. R.; Butcher, D. R.; Huang, W.; Somorjai, G. A. Size effect of ruthenium nanoparticles in catalytic carbon monoxide oxidation. *Nano Lett.* **2010**, *10(7)*, 2709-2713.

[11]Ishizaka, T.; Sakuma, T.; Kawamata, M.; Yokoyama, O.; Kato, T.; Gomi, A.; Yasumuro, C.; Toshima, H.; Fukushima, T.; Mizusawa, Y.; Hatano, T. Bottom up deposition of advanced iPVD Cu process integrated with iPVD Ti and CVD Ru. *Microelectron. Eng.* **2012**, *92*, 76-78.

[12]Kim, S. H. Low Temperature Atomic Layer Deposition of Ru Thin Films with Enhanced Nucleation Using Various Ru(0) Metallorganic Precursors and Molecular O_2. *ECS Trans.* **2011**, *41(2)*, 19-23.

[13]Kukli, K.; Kemell, M.; Puukilainen, E.; Aarik, J.; Aidla, A.; Sajavaara, T.; Laitinen, M.; Tallarida, M.; Sundqvist, J.; Ritala, M.; Leskelä, M. Atomic layer deposition of ruthenium films from (ethylcyclopentadienyl)(pyrrolyl)ruthenium and oxygen. *J. Electrochem. Soc.* **2011**, *158(3)*, D158-D165.

[14]Swerts, J.; Delabie, A.; Salimullah, M. M.; Popovici, M.; Kim, M. S.; Schaekers, M.; Van Elshocht, S. Impact of the Plasma Ambient and the Ruthenium Precursor on the Growth of Ruthenium Films by Plasma Enhanced Atomic Layer Deposition. *ECS Solid State Lett.* **2012**, *1(2)*, P19-P21.

[15]Kim, S. K.; Han, J. H.; Kim, G. H.; Hwang, C. S. Investigation on the growth initiation of Ru thin films by atomic layer deposition. *Chem. Mater.* **2010**, *22(9)*, 2850-2856.

[16]Hämäläinen, J.; Ritala, M.; Leskelä, M. Atomic layer deposition of noble metals and their oxides. *Chem. Mater.* **2013**, *26(1)*, 786-801.

[17]Yim, S. S.; Lee, M. S.; Kim, K. S.; Kim, K. B. Formation of Ru nanocrystals by plasma enhanced atomic layer deposition for non-volatile memory applications. *Appl. Phys. Lett.* **2006**, *89(9)*, 093115.

[18]Choi, S. H.; Cheon, T.; Kim, S. H.; Kang, D. H.; Park, G. S.; Kim, S. Thermal atomic layer deposition (ALD) of Ru films for Cu direct plating. *J. Electrochem. Soc.* **2011**, *158(6)*, D351-D356.

[19]Hong, T. E.; Choi, S. H,; Yeo, S.; Park, J. Y.; Kim, S. H.; Cheon, T.; Kim, H.; Kim, M. K.; Kim, H. Atomic Layer Deposition of Ru Thin Films Using a Ru(0) Metallorganic Precursor and O_2. *ECS J. Solid State Sci. Technol.* **2013**, *2(3)*, P47-P53.

[20]Popovici, M.; Groven, B.; Marcoen, K.; Phung, Q. M.; Dutta, S.; Swerts, J.; Meersschaut, J.; Van Den Berg, J. A.; Franquet, A.; Moussa, A.; Vanstreels, K. Atomic Layer Deposition of Ruthenium Thin Films from (Ethylbenzyl)(1-Ethyl-1,4-cyclohexadienyl)Ru: Process Characteristics, Surface Chemistry, and Film Properties. *Chem. Mater.* **2017**, *29(11)*, 4654-4666.

[21]Grillo, F.; Van Bui, H.; Moulijn, J. A.; Kreutzer, M. T.; Van Ommen, J. R. Understanding and Controlling the Aggregative Growth of Platinum Nanoparticles in Atomic Layer Deposition: An Avenue to Size Selection. *J. Phys. Chem. Lett.* **2017**, *8(5)*, 975-983.

[22]Li, Z.; Rahtu, A.; Gordon, R. G. Atomic layer deposition of ultrathin copper metal films from a liquid copper(I) amidinate precursor. *J. Electrochem. Soc.* **2006**, *153(11)*, C787-C794.

[23]Dendooven, J.; Ramachandran, R. K.; Solano, E.; Kurttepeli, M.; Geerts, L.; Heremans, G.; Rongé, J.; Minjauw, M. M.; Dobbelaere, T.; Devloo-Casier, K.; Martens, J. A., Vantomme, A.; Bals, S.; Portale, G.; Coati, A.; Detavernier, C. Independent tuning of size and coverage of supported Pt nanoparticles using atomic layer deposition. *Nat. Comm.* **2017**, *8(1)*, 1074.

[24]Vitos, L.; Ruban, A. V.; Skriver, H. L.; Kollar, J. The surface energy of metals. *Surf. Sci.* **1998**, *411(1-2)*, 186-202.

[25]Miskiewicz, P.; Kotarba, S.; Jung, J.; Marszalek, T.; Mas-Torrent, M.; Gomar-Nadal, E.; Amabilino, D. B.; Rovira, C.; Veciana, J.; Maniukiewicz, W.; Ulanski, J. Influence of SiO_2 surface energy on the performance of organic field effect transistors based on highly oriented, zone-cast layers of a tetrathiafulvalene derivative. *J. Appl. Phys.* **2008**, *104(5)*, 054509.

[26]Puurunen, R. L.; Vandervorst, W. Island growth as a growth mode in atomic layer deposition: A phenomenological model. *J. Appl. Phys.* **2004**, *96(12)*, 7686-7695.

[27]Grillo, F.; Moulijn, J. A.; Kreutzer, M. T.; Van Ommen, J. R. Nanoparticle sintering in atomic layer deposition of supported catalysts: Kinetic modeling of the size distribution. *Catal. Today* **2018**, 316, 51-61.

[28]Van Bui, H.; Grillo, F.; Kulkarni, S. S.; Bevaart, R.; Van Thang, N.; Van der Linden, B.; Moulijn, J. A.; Makkee, M.; Kreutzer, M. T.; Van Ommen, J. R. Low-temperature atomic layer deposition delivers more active and stable Pt-based catalysts. *Nanoscale* **2017**, *9(30)*, 10802-10810.

[29]Stevens, E.; Tomczak, Y.; Chan, B. T.; Altamirano Sanchez, E.; Parsons, G. N.; Delabie, A. Area-Selective Atomic Layer Deposition of TiN, TiO_2, and HfO_2 on Silicon Nitride with inhibition on Amorphous Carbon. *Chem. Mater.* **2018**, *30(10)*, 3223-3232.

[30]Lewis, L. N. Chemical catalysis by colloids and clusters. *Chem. Rev.* **1993**, *93(8)*, 2693-2730.

[31]Valden, M.; Lai, X.; Goodman, D. W. Onset of catalytic activity of gold clusters on titania with the appearance of nonmetallic properties. *Science* **1998**, *281(5383)*, 1647-1650.

[32]Shimizu, K. I.; Miyamoto, Y.; Satsuma, A. Size-and support-dependent silver cluster catalysis for chemoselective hydrogenation of nitroaromatics. *J. Catal.* **2010**, *270(1)*, 86-94.

[33]Joo, S. H.; Park, J. Y.; Renzas, J. R.; Butcher, D. R.; Huang, W.; Somorjai, G. A. Size effect of ruthenium nanoparticles in catalytic carbon monoxide oxidation. *Nano Lett.* **2010**, *10(7)*, 2709-2713.

[34]Nyns, L.; Delabie, A.; Caymax, M.; Heyns, M. M.; Van Elshocht, S.; Vinckier, C.; De Gendt, S. HfO_2 Atomic Layer Deposition Using $HfCl_4$/ H_2O: The First Reaction Cycle. *J. Electrochem. Soc.* **2008**, *155(12)*, G269-G273.

[35]Ratsch, C.; Zangwill, A.; Šmilauer, P.; Vvedensky, D. D. Saturation and scaling of epitaxial island densities. *Phys. Rev. Lett.* **1994**, *72(20)*, 3194

[36]Ratsch, C.; Venables, J. A. Nucleation theory and the early stages of thin film growth. *J. Vac. Sci. Technol. A* **2003**, *21(5)*, S96-S109

[37]Venables, J. A. Rate equation approaches to thin film nucleation kinetics. *Philos. Mag.* **1973**, *27(3)*, 697-738

[38]Van Hardeveld, R; Hartog, F. The statistics of surface atoms and surface sites on metal crystals. *Surf. Sci.* **1969**, *15(2)*, 189-230.

[39]Puurunen, R. L. Correlation between the growth-per-cycle and the surface hydroxyl group concentration in the atomic layer deposition of aluminum oxide from trimethylaluminum and water. *Appl. Surf. Sci.* **2005**, *245(1-4)*, 6-10.

[40]Haukka, S.; Lakomaa, E. L.; Root, A. An IR and NMR study of the chemisorption of titanium tetrachloride on silica. *J. Phys. Chem.* **1993**, *97(19)*, 5085-5094.

[41]Heo, J.; Won, S. J.; Eom, D.; Lee, S. Y.; Ahn, Y. B.; Hwang, C. S.; Kim, H. J. The role of the methyl and hydroxyl groups of low-k dielectric films on the nucleation of ruthenium by ALD. *Electrochem. Solid State Lett.* **2008**, *11(8)*, H210-H213.

[42]Delabie, A.; Sioncke, S.; Rip, J.; Van Elshocht, S.; Pourtois, G.; Mueller, M.; Beckhoff, B.; Pierloot, K. Reaction mechanisms for atomic layer deposition of aluminum oxide on semiconductor substrates. *J. Vac. Sci. Technol. A* **2012**, 30(1), 01A127.

[43]Delabie, A.; Caymax, M.; Brijs, B.; Brunco, D. P.; Conard, T.; Sleeckx, E.; Van Elshocht, S.; Ragnarsson, L. Å.; De Gendt, S.; Heyns, M. M. Scaling to sub-1 nm equivalent oxide thickness with hafnium oxide deposited by atomic layer deposition. *J. Electrochem. Soc.* **2006**, *153(8)*, F180-F187.

[44]Sneh, O.; George, S. M. Thermal stability of hydroxyl groups on a well-defined silica surface. *J. Phys. Chem.* **1995**, *99(13)*, 4639-4647.

[45]Hatton, B. D.; Landskron, K.; Hunks, W. J.; Bennett, M. R.; Shukaris, D.; Perovic, D. D.; Ozin, G. A. Materials chemistry for low-k materials. *Mater. Today* **2006**, *9(3)*, 22-31.

[46]Grill, A.; Neumayer, D. A. Structure of low dielectric constant to extreme low dielectric constant SiCOH films: Fourier transform infrared spectroscopy characterization. *J. Appl. Phys.* **2003**, *94(10)*, 6697-6707.

[47]Salh, R. In *Crystalline Properties of Silicon*; Basu, S., Ed.; InTech, 2011; Chapter 8, pp. 135-172.

[48]Zyulkov, I.; Krishtab, M.; De Gendt, S.; Armini, S. Selective Ru ALD as a Catalyst for Sub-Seven-Nanometer Bottom-Up Metal Interconnects. *ACS Appl. Mater. Interfaces* **2017**, *9(36)*, 31031-31041.

[49]Thompson, A. C.; Vaugham, D. X-Ray Data Booklet. 2nd. Lawrence Berkeley National Laboratory. **2001**.

Table of Contents Figure
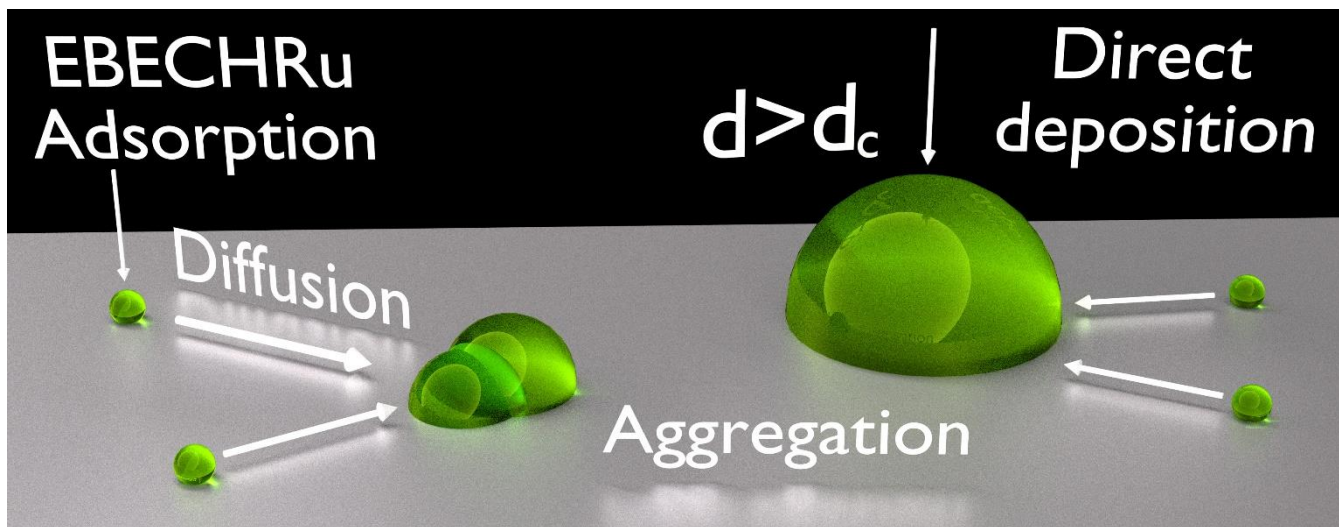
Short text for Table of Contents:

Atomic Layer Deposition of Ruthenium on dielectrics is governed by cyclic nanoparticle generation, surface diffusion, and aggregation of nanoparticles. The nanoparticle reactivity is strongly size-dependent. This insight in the growth mechanism can help tuning the morphology of the deposited material for several applications including thin film deposition, catalytic nanoparticles, and area-selective deposition.